OPEN ACCESS

University of BRISTOL

Archer, L., Neal, J., Bates, P., & House, J. (2018). Comparing TanDEM-X Data with Frequently-Used DEMs for Flood Inundation Modelling. *Water Resources Research*. https://doi.org/10.1029/2018WR023688

Publisher's PDF, also known as Version of record

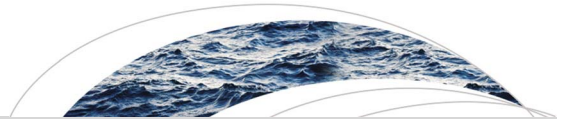Link to published version (if available):
10.1029/2018WR023688

Link to publication record in Explore Bristol Research
PDF-document

This is the final published version of the article (version of record). It first appeared online via AGU at https://agupubs.onlinelibrary.wiley.com/doi/full/10.1029/2018WR023688 . Please refer to any applicable terms of use of the publisher.

University of Bristol - Explore Bristol Research
General rights

Comparing TanDEM-X Data With Frequently Used DEMs for Flood Inundation Modeling

L. Archer[1] ⃝, J. C. Neal[1] ⃝, P. D. Bates[1] ⃝, and J. I. House[1]

[1]School of Geographical Sciences, University of Bristol, Bristol, UK

Abstract Flood risk, particularly in Small Island Developing States, is increasing. Although spaceborne Digital Elevation Models (DEMs) have provided a capacity to model flooding at the global scale, their relatively coarse resolution (~90 m) has led to a limited ability to provide fine-scale flood assessments in smaller catchments such as those in Small Island Developing States. Following the release of the TanDEM-X DEM at ~12-m resolution, the aim of this research is to determine whether TanDEM-X can improve flood estimates in comparison to Shuttle Radar Topography Mission (SRTM) and Multi-Error-Removed Improved-Terrain (MERIT) DEMs. Suitable methods to process TanDEM-X to a Digital Terrain Model (DTM) are identified through testing of seven DTMs produced through combinations of different vegetation removal approaches. Methods include Progressive Morphological Filtering and Image Classification of two TanDEM-X auxiliary data sets—a Height Error Map and Amplitude map. The LISFLOOD-FP hydrodynamic model output flood extent and water surface elevation for the TanDEM-X DTMs, SRTM, and MERIT are compared against the LiDAR model for a catchment in Fiji. The main findings show that the unprocessed TanDEM-X has improved predictive capacity over SRTM, but not MERIT. The TanDEM-X processing method combining Image Classification of the Amplitude map and Progressive Morphological Filtering produces the DTM with the highest flood model skill in comparison to all tested DEMs. This DTM reports a 12–14 percentage point higher flood model skill score than MERIT and a lower water surface elevation root-mean-square error of 0.11–0.21 m, indicating the suitability of TanDEM-X for flood modeling.

Plain Language Summary Flood risk is increasing almost everywhere, making it vital to identify at-risk areas. Highly accurate elevation data are essential for flood risk estimation, which in high-income countries is usually provided by LiDAR. However, countries such as Small Island Developing States are often reliant on spaceborne elevation data sets due to the high cost of LiDAR, despite experiencing some of the greatest levels of flood risk. These spaceborne data sets have greater errors than LiDAR and often measure vegetation canopy height instead of ground height, reducing the accuracy of flood estimates used by policy makers to assess risk. This paper aims to identify whether newly released spaceborne data set TanDEM-X could improve flood estimates in these areas by comparing flood simulations from a hydrodynamic model using TanDEM-X data with simulations based on other spaceborne data sets and LiDAR for the Ba catchment in Fiji. The results showed that TanDEM-X performs closest to the LiDAR model but only after vegetation removal processing. Further studies should be conducted in other locations, but these results indicate a possible method for improving inundation estimates in data-sparse areas. This should provide useful information for flood modeling and disaster management communities—essential given predictions of more extreme rainfall and greater exposure on floodplains.

1. Introduction

Flood risk is an area of key concern for many disaster risk reduction policies globally (Merz et al., 2010). Considering flood risk as a function of varying exposure, vulnerability, and hazard, each component must be measured to determine risk (United Nations International Strategy for Disaster Reduction, 2015). To date, hydrodynamic modeling has been the most widely used method for simulating flood inundation to aid flood risk assessment, specifically measuring flood hazard (Bates, 2012). The proliferation of Digital Elevation Model (DEM) data sets, and specifically those produced using airborne laser altimetry or LiDAR, has created a data-rich environment for flood modeling (Bates, 2004, 2012; Hunter et al., 2007; Sampson et al., 2016). Despite the numerous processes involved in simulating river flows, adding highly accurate topography data into a hydro-dynamic model is paramount for the valid simulation of flooding (Marks & Bates, 2000). A DEM is defined by Sanders (2007) as a "grid of elevation data." Most interferometry-derived DEMs are Digital Surface Models

(DSMs), measuring surface objects such as vegetation and buildings. However, a Digital Terrain Model (DTM) is required for input into a hydrodynamic model, representing "bare earth" topography (Sanders, 2007).

LiDAR is a very high-resolution data set gathered typically from aircraft, providing extremely high vertical accuracy data, but is not available globally due to high acquisition cost (Schumann et al., 2014). The Shuttle Radar Topography Mission (SRTM) DEM—a global single-pass spaceborne Interferometric Synthetic Aperture Radar (InSAR) C and X-band system flown by National Aeronautics and Space Administration in February 2000 (Rabus et al., 2003)—is a freely available global DSM data set most widely applied in flood inundation modeling where LiDAR data are unavailable (Sampson et al., 2016). The DEM was initially released as a 3-arc sec (~90 m) product and rereleased at 1 arc sec (~30 m) in 2015. It has a quoted vertical accuracy of <6 m for the X-band Synthetic Aperture Radar (SAR) and < 10 m for the C-band SAR (Farr et al., 2007; see Table 1). The main limitation of using SRTM in hydrodynamic models is that the vertical error is larger than the amplitude of most flood waves (Wilson et al., 2007). This is due to several features present in the DEM, including noise and "speckle," presence of vegetation and building artifacts, striping, and absolute bias (Rodriguez et al., 2006; Sampson et al., 2016; Yamazaki et al., 2012, 2017). Many methods have been described to increase the suitability of SRTM for flood models, including vegetation removal (Baugh et al., 2013; O'Loughlin et al., 2016), speckle and noise filtering (Yamazaki et al., 2017), hydrological corrections (Jarihani et al., 2015; Yamazaki et al., 2012), and void-filling processes (Jarvis et al., 2008; Lehner et al., 2008). Despite these known issues, SRTM is still favored in hydrodynamic modeling over other global DEM products, such as the 1-arc sec (~30-m) Advanced Spaceborne Thermal Emission and Reflection Radiometer (ASTER; Jing et al., 2013), due to better feature resolution and higher vertical accuracy (Hirt et al., 2010; Rexer & Hirt, 2014).

Most recently, Yamazaki et al. (2017) presented an error-reduced SRTM product, known as Multi-Error-Removed Improved-Terrain (MERIT) DEM. The key vertical errors present in SRTM, such as absolute bias, stripe and speckle noise, and tree height bias, are reduced using an iterative method to create a DTM from SRTM. This data set is freely available at the global scale for noncommercial purposes and global validation against ICESat and SRTM data sets suggests MERIT improves vertical accuracy (proportion of points with error < 2 m) from 39% to 58% of the globe (Yamazaki et al., 2017). Hirt (2018) most recently reported greatly reduced artifact presence in the MERIT DEM in comparison to SRTM v4.1 based on a 0.1° × 0.1° DEM tile comparison.

Despite these advances, DEM quality is arguably the main challenge for flood inundation modeling (Sampson et al., 2016). Due to the high cost of LiDAR acquisition, reliance on open-source global data sets prevails in much of the world, particularly in data-sparse areas, where a lack of topographic or ground truth data exists at a high resolution (Schumann et al., 2014).

1.1. The Case of Small Island Developing States

The need for flood hazard assessment is particularly acute in Small Island Developing States (SIDS), which are hampered by a lack of sufficiently accurate flood hazard and risk information that can be used as an evidence base by decision makers for policy implementation (Nurse et al., 2014; United Nations, 2015). The grouping of 37 island states was highlighted at the 1992 UNFCCC Rio Conference as having extraordinary risk to hazards and climate change, sharing a unique exposure and vulnerability paradigm (Barnett & Adger, 2003; Hay & Mimura, 2013; Pelling & Uitto, 2001). The combination of high hazard frequency and intensity, large exposure in relation to size and underlying vulnerability, and the limited resources and human capital to implement specialized flood mapping programs propels flood risk (United Nations International Strategy for Disaster Reduction, 2015). Recently, the exceptional risk of SIDS was reaffirmed following Hurricane Irma and Maria in the Caribbean in 2017 (National Aeronautics and Space Administration, 2017).

Previously, the limited flood modeling that has been conducted for SIDS has predominantly relied upon the use of SRTM at 90-m resolution (Albert et al., 2013; Bannari et al., 2017). Although LiDAR is the most suitable DEM for hydrodynamic modeling, its acquisition cost is prohibitive for most SIDS (Albert et al., 2013; Gesch, 2009). As well as the problems with SRTM relating to vertical accuracy, the resolution specifically limits application in SIDS, as the small size of many SIDS rivers and floodplains requires higher-resolution detail to accurately capture flood inundation characteristics. The coarse resolution also limits the ability to resolve river channels smaller than the grid cell, which applies to many SIDS rivers. Furthermore, the relative vertical

Table 1
Summary Characteristics of DEMs Used in This Study

DEM	Horizontal resolution (m)	Global relative vertical height error	Reported relative vertical height error in SIDS	Acquisition dates
TanDEM-X	~12	<2 m for low slope areas (<20%) and 4 m for high slope areas (>20%; mission specification; Rizzoli et al., 2017); 90% linear error < 2 m (Wessel et al., 2018)	Unknown	2010–2015
SRTM v4.1	~90 and ~30	16 m (mission specification) Rodriguez et al., 2006); <10 m (Farr et al., 2007); 3.6 m (Berry et al., 2007)	6.2 m for "islands" (Farr et al., 2007); 5- to 10-m Solomon Islands (Albert et al., 2013); 3-m Bahrain (Bannari et al., 2017); 25.53-m Grenada (Chirico, 2004)	2000
MERIT	~90	58% <2 m (Yamazaki et al., 2017)	Unknown	2000
LiDAR	1	5–25 cm (Baltsavias, 1999)	73.6 mm (Thomas, 2012)	2012

Note. DEM = Digital Elevation Model; SIDS = Small Island Developing States; SRTM = Shuttle Radar Topography Mission; MERIT = Multi-Error-Removed Improved-Terrain.

error of data sets such as SRTM are often larger than the elevation range of many SIDS floodplains (Chirico, 2004; Gesch, 2009). As a consequence, flood modeling in SIDS is a pronounced example of the problem with currently available DEMs for flood modeling, although the issues described are also apparent in other small data-sparse catchments in similar climates.

1.2. The TanDEM-X Mission: An Opportunity?

The TanDEM-X mission provides a potential opportunity to meet the need for a high-accuracy, global-scale DEM for flood inundation modeling, as well as specifically in SIDS. TanDEM-X is a global, spaceborne DEM, acquired at least twice between December 2010 and January 2015 using an X-band bistatic single-pass InSAR system in a public-private partnership between the German Aerospace Center (DLR) and Airbus (Rizzoli et al., 2017). Two SAR systems, TerraSAR-X and TanDEM-X, were flown in close helix orbit, between 300 and 500 m apart, enabling the acquisition of highly accurate interferograms to produce a high-precision, globally consistent DEM product (Borla-Tridon et al., 2016). The DEM has a posting of 0.4 arc sec (~12 m) and a relative vertical accuracy of 2 m in low slope (<20%) areas and 4 m in steep slope areas (>20%), providing substantial promise of improved accuracy in comparison to previous global spaceborne DEMs (Krieger et al., 2007; Rizzoli et al., 2017). TanDEM-X is a DSM, measuring surface objects (Wessel et al., 2018). The X-band SAR system has a limited capacity to penetrate vegetation, leading to volume decorrelation over densely forested areas and reduced vertical accuracy (Martone et al., 2012).

To date, a limited number of studies have validated the TanDEM-X DEM (Baade & Schmillius, 2016; Rexer & Hirt, 2016) or reported a method for processing the DSM to a DTM (Geiß et al., 2015; Mason et al., 2016; Schreyer et al., 2016). Mason et al. (2016) describe a method to use flood extent SAR images to improve the Intermediate-TanDEM-X error against LiDAR data for the potential input to a hydrodynamic model. These studies have used an Intermediate-TanDEM-X based on the first acquisition (Wessel, 2016). Most recently, Wessel et al. (2018) validated the TanDEM-X DEM against GPS data, calculating the absolute vertical error as the root-mean-square error (RMSE) between GPS and DEM heights. They reported an absolute height error of <2 m for the TanDEM-X in the test cases they examined. Thus far, results indicate a superior accuracy in comparison to SRTM and ASTER, giving the promise of an improved global DEM for a variety of geoscience applications. Nonetheless, to the best of our knowledge, no published research has yet applied TanDEM-X in a hydrodynamic modeling test case.

As a DTM is required for flood inundation models, a suitable method for TanDEM-X processing is necessary. However, application of current DTM-processing methods is likely to be unsuitable for TanDEM-X processing in isolation (Geiß et al., 2015). Schreyer et al. (2016) show that the Progressive Morphological Filtering (PMF) method was most successful when Intermediate-TanDEM-X was disaggregated to 4 m, suggesting that the method works best at a finer LiDAR-typical resolution. Geiß et al. (2015) also suggest that TanDEM-X is still too coarse for use of LiDAR processing methods, as the minimum window size (3 × 3 pixels) used in the PMF is still too large to identify small vegetation or individual buildings. On the other hand, the coarse-

scale methods applied to SRTM by Baugh et al. (2013) and Yamazaki et al. (2017) are also likely unsuitable, as the global vegetation map used to remove vegetation has a resolution of 90 m (see Simard et al., 2011) and thus does not have a high enough resolution to identify areas of vegetation smaller than 90 m that are well resolved in the TanDEM-X DEM (see Figure 2).

As a result, this paper presents the first validation results of a TanDEM-X DEM in a hydrodynamic model, as well as the first use of TanDEM-X in a SIDS context. Specifically, the key questions answered in the remainder of this paper are as follows:

1. How can artifacts be removed from TanDEM-X to create a suitable DTM for input into a hydrodynamic model?
2. Are flood estimates improved using TanDEM-X in comparison to SRTM and MERIT?

Section 2 outlines seven potential methods to process the TanDEM-X DSM to a DTM, removing vegetation artifacts using a combination of PMF and Image Classification of TanDEM-X auxiliary data sets: Height Error Map (HEM) and Amplitude (AMP), before describing the input into the hydrodynamic model LISFLOOD-FP. In section 3, the different DTMs produced using combinations of the two methods are validated against LiDAR data, as well as unprocessed TanDEM-X DSM data, SRTM DSM, and MERIT DTM, to determine the most successful DTM method for input into a hydrodynamic model. Three binary performance metrics for the modeled flood extents and the RMSE of the water surface elevation are calculated to quantitatively assess DEM accuracy relative to the LiDAR model in section 3 and discussed in sections 4 and 5.

2. Methods

2.1. Study Area

The study was conducted in Fiji—an upper-middle income SIDS located in the South Pacific (see Figure 1a). The archipelago is made up of 330 islands, of which approximately 100 are inhabited (Brown et al., 2014). The largest island, Viti Levu (see Figure 1b), has an area of approximately 10,389 km^2 and is home to ~60% of the total population (Fiji Bureau of Statistics, 2018). Fiji has a tropical maritime climate driven by trade winds, the South Pacific Convergence Zone, and the El Niño–Southern Oscillation, with 70% of annual rainfall falling between November and April during the cyclone season (Mataki et al., 2006). The island has many small rivers with a high flood frequency (McAneney et al., 2017), experiencing on average two flood events and one cyclone per year, with 97% of disasters reported between 1983 and 2012 attributable to extreme rainfall (Holland, 2014). Nonetheless, little research has estimated current or future flood hazard in Fiji using hydrodynamic modeling (Yeo et al., 2007). The most recent flood assessment for Fiji relies on MERIT data at 90-m resolution, which is relatively coarse in comparison to the scale of Fijian catchments (see Government of Fiji, 2017).

Specifically, the Ba catchment on the island of Viti Levu (Figure 1c) was chosen as the test site for three key reasons: high flood frequency, representative floodplain characteristics, and availability of LiDAR data. Recent disastrous flood events in Fiji (January 2009; 2012; March 2012; April 2018), in which the Ba catchment was worst affected, resulted in Fiji ranking third in the 2018 Global Climate Risk Index (Eckstein et al., 2017). In 2016, Fiji experienced the strongest cyclone ever recorded in the Southern Hemisphere—Cyclone Winston—affecting 62% of the population and causing damage equivalent to 20% of the nation's gross domestic product (Government of Fiji, 2016). The floodplain along the Ba river is dominated by cropland (63.85%: Fiji Bureau of Statistics, 2010), with isolated areas of vegetation and buildings, representative of most floodplains in SIDS and many other floodplains globally. It is therefore expected that the study results are likely to be replicable in other floodplains. The 21.72-km river reach in Figure 1c was chosen for the model domain as LiDAR data were available. The LiDAR data were collected and preprocessed to a DTM in 2012 through collaboration with the Secretariat of the South Pacific and the World Bank (Thomas, 2012) and were obtained for this study by Dr. Nicholas Rollings at the University of the South Pacific. Access to LiDAR data provides a good validation data source in the absence of ground truth information, as the LiDAR has a much superior vertical accuracy than the satellite DEM products (see Table 1). The LiDAR was validated against ground truth data by Thomas (2012) for 27 locations, reporting an average absolute vertical error of 73.6 mm. As a result, the Ba catchment provides a good SIDS test case whereby TanDEM-X can be adequately validated against a benchmark.
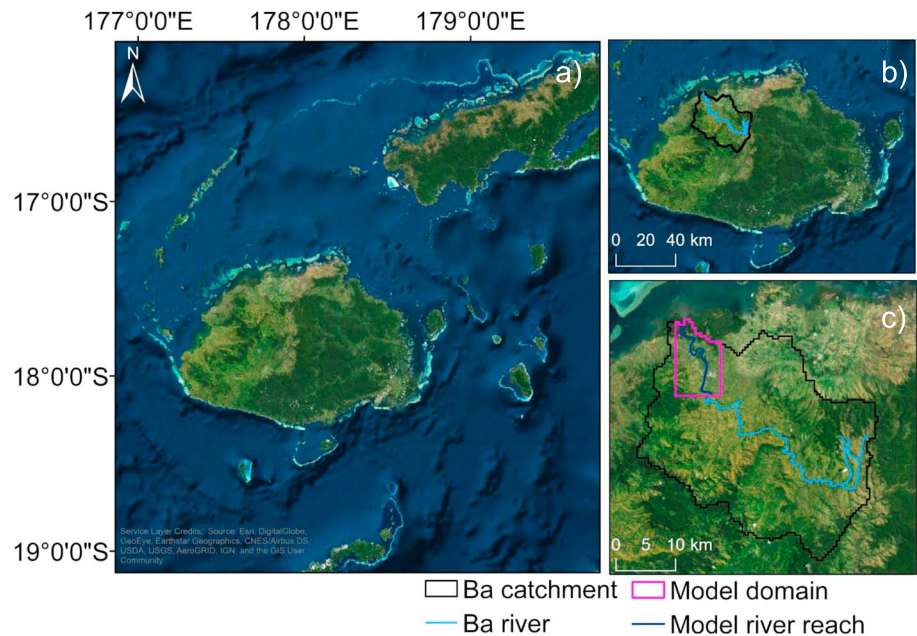
Figure 1. Map of the study site. (a) Map of Fiji. (b) Map of the Ba catchment on the main island of Viti Levu. (c) Map showing the model domain within the Ba catchment, including Ba town.
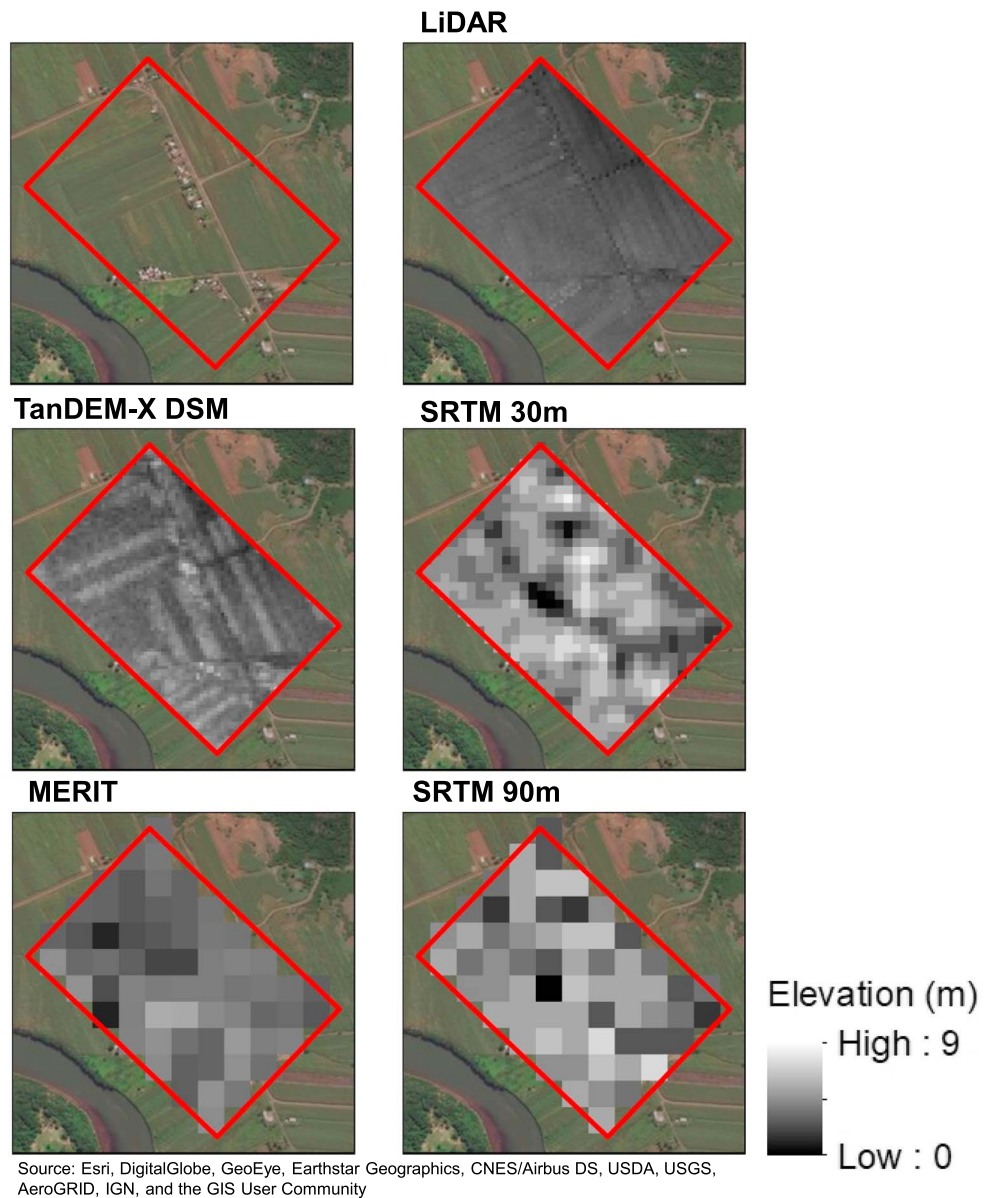
2.2. Data Sets and Preprocessing

The key DEM data sets used in this study to compare against TanDEM-X DSM and DTMs are listed in Table 1, highlighting the variation in resolution and vertical accuracy. Figure 2 demonstrates the difference in horizontal resolution across the DEMs for a section of floodplain along the Ba river, Fiji. Three modifications to TanDEM-X were conducted before processing from a DSM to a DTM. As water bodies in the TanDEM-X were incoherent with high signal disturbance, a water mask was created to exclude these pixels from further analysis, using the auxiliary Water Indication Mask included with the TanDEM-X data (Wessel, 2016) and a rasterized OpenStreetMap™ river network. The vertical coordinate system was converted from the WGS Ellipsoid to the EGM96 Geoid, aligning with the other DEMs using the free-to-use conversion software National Oceanic and Atmospheric Administration VDatum™ (v3.8). A block elevation offset of -0.5542 m was applied to the TanDEM-X, SRTM, and MERIT data sets to correspond with local mean sea level used in the LiDAR data set (Thomas, 2012).

Section 2.3 describes the PMF approach for isolated vegetation removal, and section 2.4 details the Image Classification approach used to remove large areas of vegetation, before outlining the hydrodynamic modeling and validation in sections 2.5 and 2.6. The workflow in Figure 3 shows three different method routes: PMF, Image Classification, and combination, producing seven DTMs for all possible combinations of the two methods. The seven DTM outputs are identified based on the method combination used to produce the DTM. Reference to specific tools and software is given for transparency and replicability, but the tools are based on generic operations. It is worth noting that alternatives to these tools—particularly open-source options —are available. For example, Schreyer et al. (2016) use open-source statistical programming software R packages "raster," "mmand," and "rgdal" to conduct their PMF method (R Core Team, 2018). Equivalent segmentation and Image Classification workflows can be utilized in open-source software such as Ilastik (available from https://github.com/ilastik/ilastik).

2.3. Progressive Morphological Filtering

Often used for LiDAR processing (Zhang et al., 2003), PMF was utilized by Geiß et al. (2015) and Schreyer et al., 2016 to identify buildings and vegetation artifacts in the Intermediate-TanDEM-X DEM. A PMF conducts an iteration of opening operations on an image using a sequentially increasing window size to identify artifacts of a defined smallest to largest size using two key operators: erosion and dilation (Zhang et al., 2003). The

Source: Esri, DigitalGlobe, GeoEye, Earthstar Geographics, CNES/Airbus DS, USDA, USGS, AeroGRID, IGN, and the GIS User Community

Figure 2. Diagram showing the horizontal resolution of the Digital Elevation Models used in this study for a section of floodplain along Ba river, Fiji. DSM = Digital Surface Model; SRTM = Shuttle Radar Topography Mission; MERIT = Multi-Error-Removed Improved-Terrain; USDA = U.S. Department of Agriculture; USGS = U.S. Geological Survey; CNES = Centre National d'Etudes Spatiales; IGN = Institut National De L'Information Geographique Et Forestiere; GIS = Geographic Information Systems.

erosion operator searches the pixels (x_p, y_p) within the window size (B) to find the minimum elevation to assign the defined pixel (z_p). The dilation operator searches for the maximum elevation height within the specified window using the same principle.

$$\text{Erosion} = \varepsilon_p = \left(x_p, y_p \right)_{\in B}^{\min} \left(z_p \right)$$

$$\text{Dilation} = \delta_p = \left(x_p, y_p \right)_{\in B}^{\max} \left(z_p \right)$$

An opening then sequentially applies an erosion (δ_p) and dilation (ε_p) filter to each pixel in the DEM (z_p), lowering objects smaller than the window size (B) to the minimum height value through erosion, while preserving object structure through dilation (Zhang et al., 2003).

Figure 3. Diagram showing the methodology workflow for TanDEM-X processing and the names of the output DTMs created using each combination. "OBJ" refers to objects, and "BE" refers to bare earth. HEM refers to the TanDEM-X Height Error Map, AMP to amplitude, and PMF to Progressive Morphological Filtering. The output table shows the seven different DTMs produced and which methods have been used to produce the DTM. DTM = Digital Terrain Model; AMP = Amplitude map; HEM = Height Error Map; PMF = Progressive Morphological Filtering.

$$\text{Opening} = \gamma_p = \delta_p \circ \varepsilon_p (z_p)$$

The morphological opening filter was applied using the ENVI™ (v5.4) Convolutions and Morphology tool. The opening was first performed on the unprocessed TanDEM-X DSM using a minimum window size ($B_{3\times3}$). Further openings were applied subsequently using an increasing window size of three pixels per iteration up to the maximum size ($B_{15 \times 15}$), totaling five consecutive iterations. Minimum and maximum window sizes and thus the number of iterations necessary between the two were selected based on the smallest and largest object sizes present in the TanDEM-X through visual inspection of Google Earth™ imagery. The output of each iteration identified anomalous pixels in comparison to the other pixels within the window, identifying objects of increasing size. The height difference (dh) between the output of the opening and the original DEM was established, and an elevation threshold (θ), ranging from 1 to 4 m, was applied to each height difference pixel (dh_p), classifying the pixel as an "object" if above the threshold and bare earth if below (Schreyer et al., 2016). This reduces overflattening of the terrain to the minimum pixel value and is necessary when using highly detailed terrain data (Zhang et al., 2003). Once all objects were identified, the corresponding pixels were removed from the unprocessed TanDEM-X DSM, with the remaining pixels considered bare earth.

$$\text{Bare earth} = dh_p < \theta$$
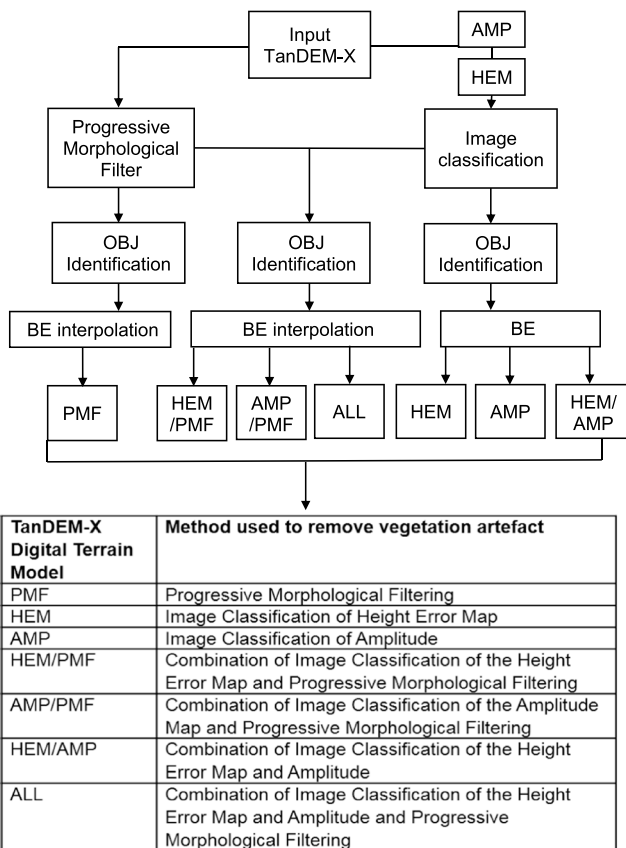$$\text{Object} = dh_p > \theta$$

Following Geiß et al. (2015) and Schreyer et al. (2016), an additional step was implemented before interpolating the bare earth pixels to create a DTM to reduce omission (false negative) and commission errors (false positive). A segmentation, using the ENVI™ (v5.4) Segmentation Image tool, was performed on each output to identify additional object pixels not identified during the opening, as omitted pixels will have the largest effect on the resulting DTM. The segmentation reclassifies bare earth as an object if a certain number of surrounding pixels within a defined neighborhood have been identified as objects, improving homogeneity of object regions. As this process results in the removal of pixels if not part of a defined region size, the objects from the segmentation output were combined with the original objects identified to retain the individual pixels identified such as isolated trees.

All identified object pixels were removed from the DEM, as the opening does not provide adequate information on the height of the object. An Inverse-Distance-Weighting interpolation is performed to estimate height values between remaining bare earth pixels to create the PMF DTM (after Schreyer et al., 2016).

2.4. Image Classification

A second method was employed focusing on the removal of large dense areas of vegetation. Two auxiliary data sets that accompany the TanDEM-X data were utilized to identify objects in this method: a Height Error Map and a map of Amplitude. The HEM, which represents the height standard deviation, is derived using interferometric coherence (Wessel, 2016). The AMP represents radar backscatter as a mean value for all the calibrated amplitudes between SAR images. These auxiliary data sets were chosen for two reasons. First, both data sets provided the highest correspondence between high values and vegetated areas in the study area based on visual inspection of Google Earth™ imagery from the time period of TanDEM-X acquisition. Second, Martone et al. (2018) suggest that areas of low interferometric coherence in the TanDEM-X data correlate with vegetated areas, due to an increase in volume decorrelation. As the HEM is derived using interferometric coherence, this data set is a suitable proxy in the absence of raw estimates of interferometric coherence.

Table 2
Confusion Matrices Using Ground Truth Regions of Interest to Determine Image Classification Accuracy of the TanDEM-X HEM and AMP

Matrix	Forest	Mangrove	Cropland	User accuracy
HEM				
Forest	82.23	40.20	2.35	41.42
Mangrove	17.77	53.62	6.23	73.70
Cropland	0	6.17	91.42	96.69
Producer accuracy	82.23	53.62	91.42	
AMP				
Forest	59.91	2.83	25.97	29.93
Mangrove	0	96.83	1.75	96.56
Cropland	40.09	0.34	72.28	90.03
Producer accuracy	59.91	96.83	72.28	

Note. Each matrix value refers to percentages of pixels classified in each class, as well as overall producer and user accuracy in percent. HEM = Height Error Map; AMP = Amplitude map.

An Image Classification method using the ENVI™ (v5.4) Supervised Image Classification workflow was used to classify the HEM and AMP to define large regions of vegetation. A supervised classification uses training data that is representative of a specific land use class to determine areas of the corresponding data set that can be identified as the same class (Canty, 2014). Areas of (i) dense vegetation, (ii) mangrove, and (iii) cropland were identified and selected from Google Earth™ imagery to create the training data regions representative of each land use class. Cropland was used as a proxy for bare earth, instead of an airplane runway or another land use class, as this was the dominant land cover in the region, and other more suitable land use cover was not present in the domain. The corresponding pixels in these regions for each map were then used to classify the remaining pixels using a maximum likelihood classification based on the discriminant function by Richards (1999). The class defined using the training data is *i*, *x* refers to the data set, where *n* is the number of bands, $p(w_i)$ refers to the probability that class (w_i) occurs in the DEM, Σi is the determinant of the covariance matrix of the data in each class (w_i), and m_i the mean vector.

$$g_i(x) = 1n\ p(w_i) - \frac{1}{2}\ 1n\ |\Sigma i| - \frac{1}{2}(x - m_i)^T \Sigma_i - 1(x - m_i)$$

To determine the accuracy of the Image Classification, a confusion matrix was calculated for the HEM and AMP classification outputs, using three alternative regions of interest to the regions used as training data for the classification, referred to as "ground truth" regions (see the supporting information; Congalton, 1991). The confusion matrices for both classifications are shown in Table 2, calculated using the ENVI™ (v5.4) postclassification Confusion Matrices Using Ground Truth ROIs tool, demonstrating the percentage of pixels classified and the producer and user accuracy of each class. Producer accuracy refers to the probability of correct classification, and user accuracy refers to the probability that a given class classification is truly that class (Canty, 2014). Overall, the results demonstrate a 79.11% accuracy for the HEM and a 78.17% accuracy for the AMP by calculating correct pixels/total pixels. The Kappa coefficient for both confusion matrices was 0.64, calculated to determine the agreement between the ground truth and classification values, whereby 1 equals complete agreement and 0 equals no agreement (Congalton, 1991). These results suggest good overall image classification accuracy, signifying that the objects identified by the process are representative. Nonetheless, Table 2 shows limited capacity to classify between mangrove and forest in the HEM classification, suggesting the height error values for both classes are similar, thus reducing the overall classification accuracy. Table 2 shows a relatively reduced capacity to distinguish between forest cover and cropland in the AMP, although mangrove classification is superior, suggesting that amplitude values between forest and mangrove cover are dissimilar.

For the purpose of object identification, a good classification between objects (in this case forest or mangrove) and bare earth (in this case cropland) is required. Despite the little difference in overall classification accuracy, the HEM may have a higher capacity to accurately identify objects in comparison to the AMP due to the performance of the "cropland" classification. Both the HEM and AMP have limited user accuracy for forest, suggesting forest that classification has the most limited classification. Despite the good accuracy of the Image Classification, the external data set 300-m resolution Climate Change Initiative 2015 Land Cover Classification (Available from: https://www.esa-landcover-cci.org/) was used to further assess the general classification percentages for each land use, finding cropland as the dominant classification (see the supporting information). Running an unsupervised classification also showed <10 percentage point differences in land cover classification.

Once validated, the areas identified as forest or mangrove in the classification were identified as objects and removed from the DEM. As the objects identified in this method removed much larger areas than in the PMF, the Inverse-Distance-Weighting interpolation was maintained for localized areas but an Elevation Void-Filling function in ArcMap™ (v10.5) was used to interpolate larger areas using a plane fitting approach.

2.5. Hydrodynamic Modeling

As demonstrated in Figure 3, seven DTMs were produced using PMF, the HEM, and AMP in isolation and combination. All seven DTMs, as well as the unprocessed TanDEM-X DSM, LiDAR, SRTM, and MERIT DEMs, were used as the topography input into the subgrid variant of the hydrodynamic model LISFLOOD-FP (Neal et al., 2012). The MERIT and SRTM 90-m models were run in 0.67 min and SRTM 30 m in 9.5 min. All other models were run at the native TanDEM-X resolution (~12 m) with an average run time of 140 min. The LiDAR model was run at the resolution of TanDEM-X, not at native resolution (~1 m), as minimal improvement is typically shown with resolutions below this at the cost of a large computational expense by an order of magnitude every time DEM resolution is reduced by half (e.g., Savage et al., 2015, found no improvement in simulation accuracy below 50-m resolution). This does mean that the other DEMs were compared to the coarsened LiDAR, but this was an acceptable limitation given these justifications. Key model inputs required by the hydrodynamic model include topography-derived variables and boundary conditions (Bates et al., 2013). The input variables to the model were identical except for the topography-derived variables (DEM, bank heights, and bed elevation). Manning's coefficient friction was set at 0.035 for the channel and 0.040 for the floodplain in all models based on a typical agricultural floodplain.

The river channel in the subgrid variant of LISFLOOD-FP is estimated using bank heights, bed heights, and channel width information (Neal et al., 2012). Bank heights were extracted along the perimeter of the river channel in the DEM. Due to the relatively small size of the river reach, the widths were measured at a series of points along the river channel whose location was identified using Google Earth™ imagery. Bed elevation was estimated using bank height, river width, and return period discharge estimates, such that the channel water level would closely match the banks height at a given return period flow (1 in 2 years in this case: Pickup & Warner, 1976). A binary channel mask (1 = water and 0 = data) was also employed to overlay the water-masked river channel in the unprocessed TanDEM-X DSM and DTMs, signaling to the model to start 2-D floodplain flow at the channel boundary.

The LISFLOOD-FP model requires an input discharge at the upstream boundary and water surface elevation at the downstream boundary (Bates et al., 2013). The downstream boundary of the model was fixed at 0 m, set at local mean sea level corresponding with the DEMs. The upstream boundary was located 21.72 km upstream. Due to a lack of accurate and complete flow gauge data for the Ba river (Yeo et al., 2007), a historical flood event time series could not be used to simulate discharge in the model. Thus, a regional flood frequency analysis outlined by Smith et al. (2015) was conducted to simulate peak discharge estimates at various return periods based on available flow data in hydrologically similar catchments and rainfall data from the Fiji Meteorological Office. This method was also utilized in the Government of Fiji's (2017) Climate Vulnerability Assessment.

A hydrograph was created using the rational method, which takes the peak discharge estimates for the 50-, 25-, and 10-year return period events, and the catchment time to concentration of 5.43 hr to produce a hydrograph (see the supporting information). The total simulation duration was set at 48-hr following historical events in the region. Time to concentration was calculated using the velocity method detailed in Woodward et al. (2010). This method calculates time to concentration by the sum of travel times from the most hydraulically distant point in the watershed to the downstream outlet, assuming three flow types: sheet flow, shallow concentrated flow, and open channel flow. Three return period events were simulated as larger "valley-filling" floods can be less sensitive to floodplain dynamics and may therefore be less sensitive to DEM error (Schumann et al., 2009).

Models using all 11 DEMs for the three return period events were simulated, and a maximum flood extent map was produced for each model run.

2.6. Model Evaluation

The flood model outputs were measured using binary pattern-matching performance metrics based on a contingency table, commonly used in flood modeling to validate model outputs (Hunter, 2005; Pappenberger et al., 2007; Schumann et al., 2009; Stephens et al., 2014). As the LiDAR model is considered as the "truth" for the purposes of this study, the DEM that produces the flood extent and water surface elevation with the closest fit to the LiDAR model is considered the most successful candidate. The LiDAR model is not necessarily an exact representation of floodplain topography. Yet for the purposes of DEM comparison,

this was considered an acceptable limitation as the LiDAR data are likely to provide the most reliable benchmark available. A contingency table, as described in Stephens et al. (2014), was used to assess whether a pixel in the model is correctly/incorrectly identified as wet/dry (see the supporting information). The metric was then calculated using the number of pixels in each category of the contingency table (A, B, C, and D) to assess accuracy.

Hunter (2005) and Stephens et al. (2014) stress the importance of calculating several binary metrics when assessing model performance, as individual metrics can present a bias to models under predicting, over predicting, or with large dry domains. Three binary metrics were calculated, as well as the RMSE of the model water surface elevation, to determine the most successful model. The Critical Success Index, or $F^{<1>}$ score, is the most commonly used binary metric when assessing flood model skill, and the $F^{<2>}$ and $F^{<3>}$ scores penalize underprediction and overprediction, respectively (Stephens et al., 2014). If a similar pattern is shown in all three metrics, then the Critical Success Index is unlikely to display bias toward over prediction in these models (Hunter, 2005).

$$CSI = \frac{A}{A+B+C}$$
$$F^{<2>} = \frac{A-C}{A+B+C}$$
$$F^{<3>} = \frac{A-B}{A+B+C}$$

Stephens et al. (2014) suggest that calculating the RMSE of water surface elevation between a model and observation provides a useful metric to communicate the depth prediction skill of a model. The RMSE is a common statistical accuracy measure used to determine error between predicted and observed values (Wessel et al., 2018).

$$RMSE = \sqrt{\frac{\sum_{i=1}^{n}(P_i - O_i)^2}{n}}$$

3. Results

The maximum flood extents for each model for the 50-year return period flood event are outlined, followed by the metric results for all three return period events.

### 3.1. How Well Does the Unprocessed TanDEM-X DSM Perform?

The maximum flood extents shown in Figure 4a demonstrate that the unprocessed TanDEM-X DSM has an improved capacity to model flooding in comparison to SRTM, suggesting improved DSM quality over SRTM. The metric scores outlined in Table 3 also indicate a marked improvement and are echoed by the $F^{<2>}$ and $F^{<3>}$ scores outlined in the supporting information.

The MERIT DTM has higher skill than both SRTM and TanDEM-X DSMs, and SRTM 30 m does not improve results significantly in comparison to SRTM at 90 m, indicating the relative importance of a DTM over horizontal resolution. Two key areas that are flooded in the LiDAR model and the MERIT DTM but not TanDEM-X DSM and SRTM are the mangroves at the downstream boundary and the dense patches of vegetation along the river on the floodplain, demonstrating the impact of vegetation artifact on model performance. The metrics were therefore calculated for the 50-year model including and excluding the mangroves at the downstream boundary and the 25- and 10-year models were calculated excluding mangroves, as the poor accuracy over mangrove areas reduces the ability to assess the DTMs upstream, which is of more interest in flood risk assessment. The mangroves provide a tough test case for an X-band InSAR such as TanDEM-X and are inherently difficult to model. Mangroves have a closed canopy meaning little ground return is available for the area (Mitchell et al., 2007), so the TanDEM-X DSM has a particularly difficult time measuring bare earth. Furthermore, LiDAR ground truthing was not conducted by Thomas (2012) in the mangroves, so the authors cannot determine the accuracy of the LiDAR in this location. This creates a second justification for removal of the mangrove areas in the analysis, as the benchmark LiDAR accuracy over these areas is unknown. This study

a)
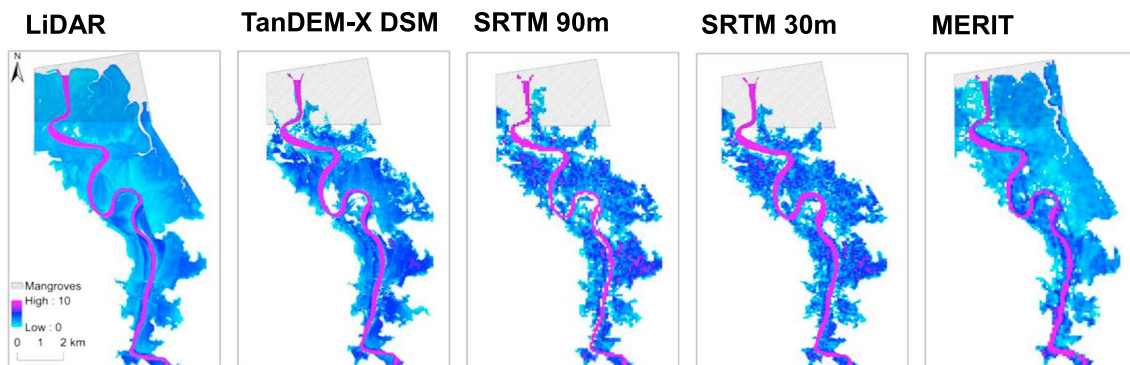
b)
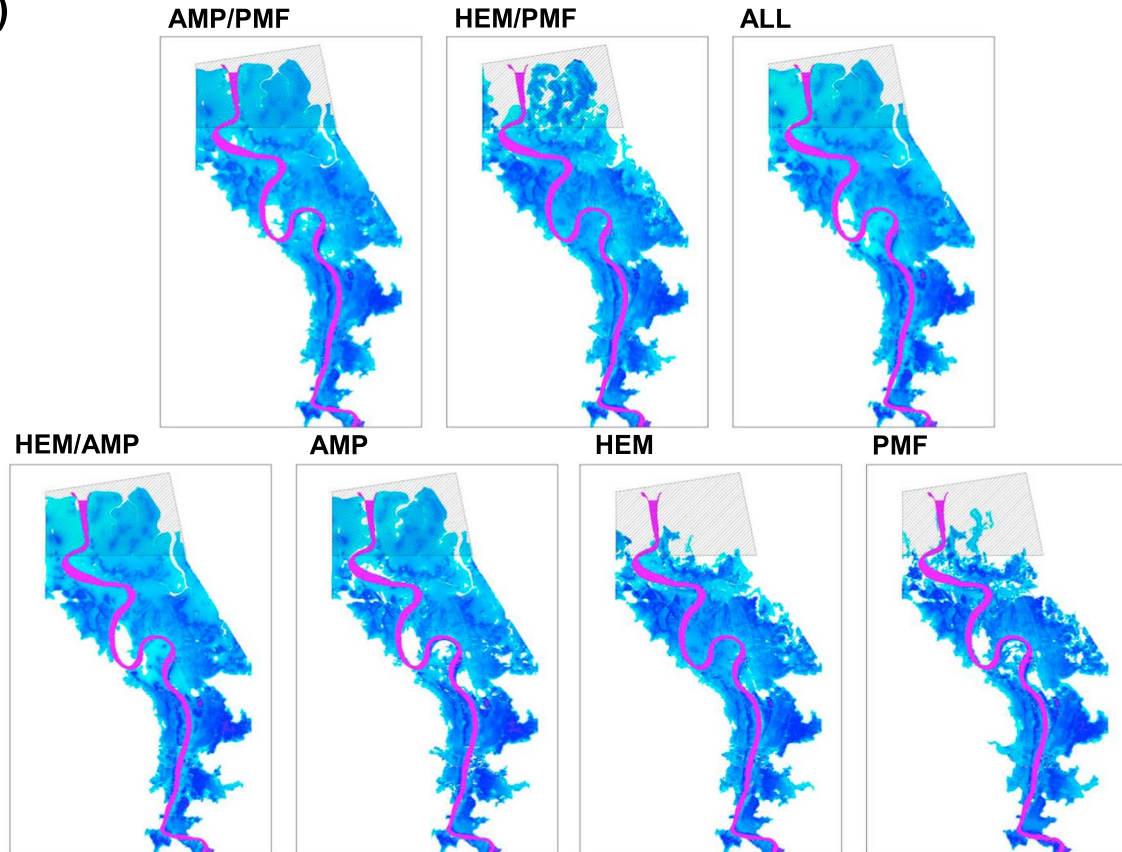
Figure 4. (a) Modeled flood extents for the LiDAR, TanDEM-X DSM, SRTM, and MERIT DEMs for the 50-year return period event. (b) Modeled flood extents for the seven TanDEM-X DTMs for the 50-year return period event. Acronyms for the DTMs correspond with the method used: AMP describes use of TanDEM-X Amplitude map, HEM describes use of TanDEM-X Height Error Map, and PMF Progressive Morphological Filtering. DEM = Digital Elevation Model; DTM = Digital Terrain Model; DSM = Digital Surface Model; SRTM = Shuttle Radar Topography Mission; MERIT = Multi-Error-Removed Improved-Terrain.

does not suggest that the methods detailed can entirely remove mangrove regions, and the results show poorer accuracy in mangrove-covered areas. An artificial boundary either side of the mangroves at the downstream boundary is produced due to the constrained model domain (see Figure 1c), dictated by the LiDAR data coverage used as the benchmark.

Table 3
The Left of the Table Shows the Scores for Each DEM for the Critical Success Index Binary Performance Metric for Each Return Period When Compared to the LiDAR Flood EXTENT Which Is Taken Here as a Benchmark

DEM	Critical success index (0–1)				Water surface elevation RMSE (m)			
	50 years				50 years			
	Including mangroves	Excluding mangroves	25 years	10 years	Including mangroves	Excluding mangroves	25 years	10 years
TanDEM-X DSM	0.61	0.75	0.70	0.57	0.72	0.75	0.65	0.50
SRTM 90 m	0.58	0.69	0.63	0.48	0.88	0.95	0.84	0.66
SRTM 30 m	0.58	0.71	0.65	0.51	0.85	0.91	0.81	0.65
MERIT	0.77	0.77	0.72	0.60	0.63	0.68	0.62	0.52
PMF	0.64	0.77	0.71	0.58	0.68	0.70	0.61	0.46
HEM	0.67	0.84	0.78	0.63	0.62	0.62	0.55	0.43
AMP	0.86	0.84	0.80	0.66	0.51	0.59	0.54	0.45
HEM/PMF	0.84	0.89	0.85	0.69	0.52	0.53	0.49	0.42
AMP/PMF	0.90	0.89	0.85	0.74	0.42	0.49	0.41	0.37
HEM/AMP	0.90	0.88	0.83	0.65	0.52	0.58	0.55	0.43
ALL	0.90	0.88	0.83	0.67	0.51	0.57	0.54	0.48

Note. Scores range from 0 (*no agreement*) to 1 (*total agreement*). The right side of the table shows root-mean-square error (RMSE) between the water surface elevation of each DEM flood output and the LiDAR model. The higher the score the higher the error, reported in meters. The red highlighted boxes indicate the worst performing DEM in the category, and the green highlighted boxes indicate the best performing DEM. DEM = Digital Elevation Model; SRTM = Shuttle Radar Topography Mission; MERIT = Multi-Error-Removed Improved-Terrain; PMF = Progressive Morphological Filtering; HEM = Height Error Map; AMP = Amplitude map.

3.2. TanDEM-X DTM Comparison Analysis

Figure 4b shows all seven TanDEM-X DTM model flood extents, produced using combinations of the Image Classification of the HEM and AMP and PMF as described in Figure 3.

The PMF DTM, produced using only Progressive Morphological Filtering, is the worst performing TanDEM-X DTM when input into the hydrodynamic model, with the lowest agreement of the seven DTMs in maximum flood extent simulation and Critical Success Index (Table 3). The PMF DTM is also the worst performing DTM created using one method.

The AMP/PMF is overall the most consistently superior DTM when visually comparing flood outputs as well as for overall model skill, despite the remaining presence of artifact along the channel edge in the model output (see Figure 4b).

DTMs created using a combination of methods have higher agreement with the LiDAR model when visually comparing and assessing binary metric performance in comparison to DTMs created using one method. AMP/PMF is the most successful combination method. HEM/PMF has higher model skill than HEM/AMP and ALL, except for when mangroves are included in binary metric calculation for the 50-year event. There is little difference between HEM/AMP and ALL DTMs metric performance in Table 3 and the visual flood extents.

In general, when PMF is combined with Image Classification of either the Height Error Map or Amplitude (AMP/PMF and HEM/PMF) the accuracy of the flood extent is improved in comparison to when the methods are used in isolation or in other combinations. This suggests that a combination of a coarse and fine processing methods produces the best performing DTMs overall.

3.3. TanDEM-X DTM Selection

When analyzing all 11 flood extents in Figure 4 and Table 3, AMP/PMF was the DTM selected as the most successful candidate for flood inundation and water surface estimation in comparison to the LiDAR model. This method is therefore considered the most suitable TanDEM-X processing method, creating a DTM with a higher capacity to model flooding in comparison to the other TanDEM-X DTMs and MERIT DTM, as well as the unprocessed TanDEM-X and SRTM DSMs.
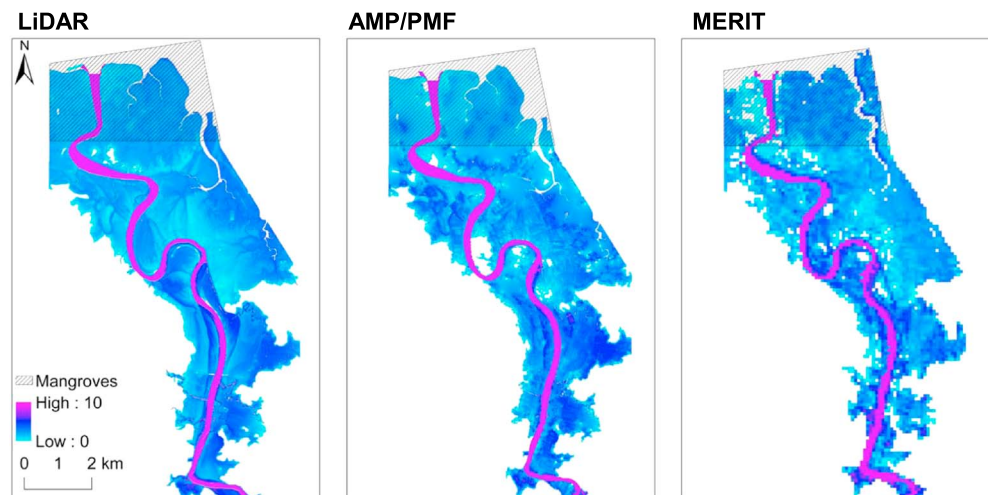
Figure 5. Modeled flood extents of the two TanDEM-X Digital Terrain Models AMP/PMF and MERIT in comparison to the LiDAR model for the 50-year return period event. AMP = Amplitude map; PMF = Progressive Morphological Filtering; MERIT = Multi-Error-Removed Improved-Terrain.

The AMP/PMF DTM, as well as the other combination TanDEM-X DTMs, has a higher model skill than the MERIT DTM. As the MERIT DTM is currently most often used in data-sparse flood inundation modeling whereby LiDAR data are unavailable, it is important to directly compare the results of the AMP/PMF DTM to the MERIT DTM to consider the scale of improvement shown (see Figure 5). The AMP/PMF DTM has a Critical Success Index score of 12–14 percentage points higher than the MERIT DTM (Table 3) and performs consistently highest when tested for under and over prediction (see the supporting information), showing improved flood extent model skill. Water surface elevation prediction skill is also greater, with a RMSE of 0.11–0.21 m lower than the MERIT DTM (Table 3).

4. Discussion

Consistently for all four metrics, TanDEM-X DSM has a higher flood estimation accuracy than the SRTM DSMs but worse than the MERIT DTM and the TanDEM-X DTMs. Crucially, just because TanDEM-X has a higher resolution and higher average vertical accuracy, preprocessing to a DTM is still required to remove surface artifacts, aligning with previous review of SRTM and LiDAR in hydrodynamic modeling (Bates, 2004, 2012; Sampson et al., 2016).

TanDEM-X has a higher accuracy than SRTM in comparison to LiDAR for three key reasons: (i) acquisition date, (ii) spatial resolution, and (iii) vertical accuracy. As TanDEM-X was acquired between 2010 and 2015 (Rizzoli et al., 2017), and the LiDAR data were acquired in 2012 (Thomas, 2012), the characteristics of the floodplain captured are likely to be more similar in comparison to SRTM, which was acquired in 2000 (Rabus et al., 2003), following changes in land use during the period (Yeo, 2015). Furthermore, as TanDEM-X has a higher spatial resolution and a higher specified vertical accuracy than the SRTM mission (Rizzoli et al., 2017; Wessel et al., 2018), the finer-scale characteristics of the floodplain morphology will be better represented than in the SRTM.

Although the MERIT DTM is an error-reduced SRTM product at 90 m, the unprocessed TanDEM-X DSM has a lower flood prediction accuracy for flood extent and water surface elevation. It is apparent in Figure 4a that the main areas that remain dry in TanDEM-X but not in the LiDAR or MERIT DTMs are the mangroves at the downstream boundary and large patches of tall vegetation along the floodplain, leading to poorer flood extent prediction skill. Water surface elevation RMSE in the TanDEM-X DSM is also higher than the MERIT DTM, likely due to vegetation artifacts blocking key flow pathways across the floodplain surface (Mason et al., 2011). This highlights the pronounced presence of vegetation artifacts in the TanDEM-X, largely because the X-band SAR system has limited penetration of the canopy (Martone et al., 2018; Wessel et al., 2018). Therefore, presence of mangroves strongly affects the overall results potentially masking the

capability of the DEM in upstream areas. The skill of the model in these upstream areas is in fact more critical as these are the more populated areas and thus of more interest in flood risk assessment, especially considering the accuracy of the LiDAR benchmark in the mangrove area is also unknown. Although mangroves appear to have been removed in Yamazaki et al.'s (2017) MERIT DTM using height information indicated in the ~90-m resolution global vegetation height map (Simard et al., 2011), the methods used to remove these are coarse scale and thus not suitable for TanDEM-X. Therefore, further investigation is required to optimize mangrove-removal for TanDEM-X for the DEM to be applicable for hydrodynamic modeling at the global scale.

4.1. TanDEM-X DTM Processing: A Balance

The DTM produced using the AMP/PMF method is the most suitable candidate for modeling both flood extent and water surface elevation in comparison to the LiDAR model, followed by HEM/PMF. This underpins the argument that previously established DEM processing methods used for both fine-resolution LiDAR data (Schreyer et al., 2016; Zhang et al., 2003) or coarse-scale InSAR data (Baugh et al., 2013; Yamazaki et al., 2017) cannot be directly applied to the TanDEM-X data in isolation, indicating the need for a fine balance between coarse- and fine-scale processing. When the methods are used in isolation, the resulting DTM still contains too many artifacts to provide a smooth representation of bare earth topography, as shown in the binary metric performance for PMF, AMP, and HEM DTMs in comparison to AMP/PMF, HEM/PMF, HEM/AMP, and ALL DTMs (see Table 3). The results are also consistent with Geiß et al.'s (2015) argument that the spatial resolution of TanDEM-X still limits the use of PMF in isolation, as even the smallest window size (3 × 3 pixels) is larger than individual trees or buildings, with the PMF DTM ranking as the worst performing TanDEM-X DTM.

Initial assumptions would suggest that the more artifacts identified and removed from the DEM, the smoother and thus more representative the resulting DTM, justifying the iterative procedure (Geiß et al., 2015; Yamazaki et al., 2017). However, the AMP/PMF is clearly the most consistently superior DTM across all metrics when compared against the other combination DTMs, despite using fewer methods to remove artifact. Although the ALL DTM, whereby all three methods are combined, has particularly good skill for the 50-year return period event, this is likely influenced by the valley-filling flood effect, whereby larger floods are less sensitive to floodplain error, meaning little difference in performance is identified using the binary metric assessment between the combination methods (see Table 3). The ALL DTM also shows superior performance when mangroves are included in binary metric calculation for the 50-year return period event, suggesting that the capacity to flood the mangrove area may provide a bias in the results toward the ALL DTM in comparison to other DTMs, leading to an overestimation of model skill.

Results showing that HEM/AMP and ALL DTMs have little difference between metric results also reinforces the need for a balance between coarse and fine-scale artifact removal, as the results indicate that adding another method to remove artifact does not necessarily improve the output DTM. This is echoed by Baugh et al.'s (2013) comparison with Coe et al. (2008) and Paiva et al.'s (2011) SRTM vegetation removal studies, indicating that larger modification does not necessarily improve accuracy. Therefore, although a combination of methods improves TanDEM-X DTM flood prediction accuracy over methods in isolation, a delicate balance between fine- and coarse-scale processing is required to process TanDEM-X data, as the AMP/PMF DTM (and to a lesser extent HEM/PMF DTM) demonstrate the best performance overall for the various-sized flood events and particularly for the smaller events whereby DEM error is more influential (Schumann et al., 2009).

Despite the successful use of interferometric coherence estimates to detect vegetation in the TanDEM-X DSM by Martone et al. (2018) and the superior classification accuracy of the HEM in comparison to the AMP (see Table 2), the finding that AMP/PMF has a better flood prediction accuracy than when the HEM—an error map created using interferometric coherence—is used to produce the output DTMs HEM, HEM/PMF, and HEM/AMP suggests that interferometric coherence is not necessarily the most useful indicator for vegetation artifact at this site when compared to the AMP. Perhaps because the HEM is derived using interferometric coherence as opposed to being a direct indicator (Wessel, 2016), the capacity to remove vegetation artifact using the HEM as opposed to true interferometric coherence estimates may be different. As AMP/PMF is the most suitable DTM candidate, the AMP clearly has a good capacity to identify vegetation objects despite the Image Classification showing lower accuracy between "forest" and cropland classification. Without

information on suggested amplitude and interferometric coherence values for both forest and "mangrove," explanation for this result is limited, so further investigation into the use of amplitude as an indicator of surface artifacts in the TanDEM-X DSM should be conducted.

4.2. Future Application

This study outlines the first results using TanDEM-X as an unprocessed DSM and a processed DTM in a hydrodynamic model. These results demonstrate that when TanDEM-X is processed to produce a DTM using a combination of vegetation removal methods, it greatly improves flood estimates in comparison to both SRTM and MERIT, demonstrating potential for use of higher resolution, globally available TanDEM-X data for flood modeling. Specifically, the TanDEM-X AMP/PMF DTM led to the greatest improvement in the simulation of both flood extent and water surface elevation.

This study only investigated the TanDEM-X DSM and DTMs in one catchment, despite the argument that model sensitivity to a DEM differs between catchments, which may lead to divergent conclusions when applied elsewhere. The method was not applied to another study area due to limited access to TanDEM-X data, meaning there are several ways TanDEM-X and the AMP/PMF method should be tested in other sites to validate the findings regarding TanDEM-X performance in this study. Simulated flood extents using both the TanDEM-X DSM and AMP/PMF DTM should also be validated against synoptic inundation observations (e.g., SAR or optical imagery) and other ground based validation data (e.g., level gauges and water marks) to determine whether TanDEM-X has suitable predictive skill in comparison to actual flood events (Bates, 2012). Yet, despite these caveats, the accuracy metrics in this paper are concurrent with arguments in the literature; that is, the results show that having a DTM improves prediction over DSM (Bates, 2012) and higher-resolution DTMs produce more accurate topographic representations and hence better flood estimates (Horritt & Bates, 2001; Sanders, 2007). Therefore, it is likely that TanDEM-X will have a capacity to improve flood estimates in other locations with similar characteristics, despite additional work being needed to verify the degree of the improvement. Further processing is also likely to be required in urban catchments due to presence of building artifacts in the TanDEM-X DSM.

There are key barriers that are likely to reduce the use and further validation of this TanDEM-X AMP/PMF DTM approach globally and also specifically in SIDS. The TanDEM-X data are not open-source but available through the German Aerospace Center (DLR) following an application process for scientific use and a cost of ~€100 per tile (Wessel, 2016). As it is much easier to access the free SRTM or MERIT, for example, MERIT has been released free for noncommercial use by Yamazaki et al. (2017), a scientific community familiar with these data sets is likely to continue using these DEMs until access to TanDEM-X is easier and/or proved to be more effective (i.e., worth the additional effort to both get the data and apply new methods). This is specifically likely to hamper TanDEM-X application in SIDS due to the limited capacity or resources to implement new methodologies and data sets to existing flood risk assessment (Yeo, 2015). The fact that almost 2 years after the release of the TanDEM-X DEM (Moreira, 2017), there has been no study demonstrated the suitability of TanDEM-X for flood modeling until now, despite this being an obvious application area, is an indication of these access and capability issues.

It is worth noting that a suitable error-reduced DTM from SRTM was only produced 17 years after the SRTM DSM release despite the free availability of SRTM (Schumann et al., 2014). Without wider accessibility of TanDEM-X, the capabilities of TanDEM-X for flood modeling may be realized much more slowly than SRTM, and quality of DEM data will remain the key limitation to high-accuracy hydrodynamic modeling for years to come (Sampson et al., 2016; Schumann et al., 2014). This would be a significant limitation to future flood modeling in data-sparse areas, and specifically SIDS, whereby better flood risk assessment is urgently needed (Hay & Mimura, 2013; Nurse et al., 2014). We note that the release of 90-m TanDEM-X in October 2018 (DLR, 2018) may accelerate the uptake of the data for flood applications, although as was the case with SRTM our results suggest that a vegetation removal algorithm will be needed.

Thus, it is timely that this study provides an insight into the competency of TanDEM-X for flood modeling, highlighting key methodological approaches to process the data and identifying gaps for further investigation. Continued exploration of other potential artifacts in the TanDEM-X DSM such as possible striping error causing a repetitive undulation in the elevation heights are necessary but were beyond the scope of this study. Following the analysis of TanDEM-X in Ba, Fiji, there is confidence that the results from this study will

be broadly applicable to other floodplains that share similar characteristics. Nevertheless, the AMP/PMF method should be applied in other study sites to validate the results of this study.

5. Conclusion

The aim of this paper was to identify whether an appropriate method can be used to process TanDEM-X for use in a hydrodynamic model and whether this improves flood estimates in comparison to already existing global DEMs SRTM and MERIT in a SIDS context. The unprocessed TanDEM-X DSM did improve flood estimates over the SRTM DSMs when input into a hydrodynamic model, but not the MERIT DTM, emphasizing that although TanDEM-X has a higher resolution, this does not negate the need for surface artifact processing from a DSM to a DTM. This study also demonstrates the first application of a method to process the TanDEM-X DSM to a DTM for use in a hydrodynamic model. The results identified that the method combining the Image Classification of the TanDEM-X auxiliary Amplitude map and Progressive Morphological Filtering (AMP/PMF DTM) is the most appropriate vegetation removal method for TanDEM-X. When using the AMP/PMF method to produce a DTM, the Critical Success Index measuring flood extent accuracy relative to the LiDAR model is 12–14 percentage points higher than the MERIT DTM, and the water surface elevation RMSE is 0.11–0.21 m lower than the MERIT DTM. This indicates that when TanDEM-X is processed using this method, flood estimates are greatly improved in comparison to already existing DEMs used in flood modeling. This provides substantial promise for TanDEM-X in hydrodynamic modeling, specifically in SIDS whereby a high-resolution but less expensive DEM is critical to improve flood risk assessment in relatively small catchments typical in the region, under both current and future extreme rainfall scenarios. The improved capabilities for flood modeling, along with suitable methods for processing data highlighted for the first time in this study, should provide stimulus for the application of this data and approach to a range of study sites to both validate and extend the use of TanDEM-X to improve future flood modeling.

References

Albert, S., Abernethy, K., Gibbes, B., Grinham, A., Tooler, N., & Aswani, S. (2013). Cost-effective methods for accurate determination of sea level rise vulnerability: A Solomon Islands example. *Weather Climate and Society*, *5*(4), 285–292. https://doi.org/10.1175/WCAS-D-13-00010.1

Baade, J., & Schmullius, C. (2016). TanDEM-X IDEM precision and accuracy assessment based on a large assembly of differential GNSS measurements in Kruger National Park, South Africa. *ISPRS Journal of Photogrammetry and Remote Sensing*, *119*, 496–508. https://doi.org/10.1016/j.isprsjprs.2016.05.005

Baltsavias, E. P. (1999). Airborne laser scanning: Basic relations and formulas. *ISPRS Journal of Photogrammetry and Remote Sensing*, *54*(2-3), 199–214. https://doi.org/10.1016/S0924-2716(99)00015-5

Bannari, A., Kadhem, G., Hameid, N., & El-Battay, A. (2017). Small island DEMS and topographic attributes analysis: A comparative study among SRTM-V4.1, ASTER-V2.1, high topographic contours maps and DGPS. *Journal of Earth Science and Engineering*, *7*, 90–119.

Barnett, J., & Adger, N. (2003). Climate dangers and atoll countries. *Climatic Change*, *61*(3), 321–337. https://doi.org/10.1023/B:CLIM.0000004559.08755.88

Bates, P. D. (2004). Remote sensing and flood inundation modelling. *Hydrological Processes*, *18*(13), 2593–2597. https://doi.org/10.1002/hyp.5649

Bates, P. D. (2012). Integrating remote sensing data with flood inundation models: How far have we got? *Hydrological Processes*, *26*(16), 2515–2521. https://doi.org/10.1002/hyp.9374

Bates, P. D., Trigg, M., Neal, J., & Dabrowa, A. (2013). LISFLOOD-FP user manual: Version 2.0. Bristol: University of Bristol.

Baugh, C. A., Bates, P. D., Schumann, G., & Trigg, M. A. (2013). STRM vegetation removal and hydrodynamic modeling accuracy. *Water Resources Research*, *49*, 5276–5289. https://doi.org/10.1002/wrcr.20412

Berry, P. A. M., Garlick, J. D., & Smith, R. G. (2007). Near-global validation of the SRTM DEM using satellite radar altimetry. *Remote Sensing and the Environment*, *106*(1), 17–27. https://doi.org/10.1016/j.rse.2006.07.011

Borla-Tridon, D., Bachmann, M., Martone, M., Schulze, D., & Zink, M. (2016). The future of TanDEM-X: Final DEM and beyond, Proceedings of the European Conference on Synthetic Aperture Radar, Hamburg, Germany.

Brown, P., Daigneault, A., & Gawith, D. (2014). Climate change and the economic impacts of flooding on Fiji. *Climate and Development*, *9*(6), 493–504.

Canty, M. J. (2014). *Image analysis, classification and change detection in remote sensing: With algorithms for ENVI/IDL* (3rd ed.). Florida, USA: CRC Press.

Chirico, P. G. (2004). An evaluation of SRTM, ASTER and Contour-based DEMs in the Caribbean region, proceedings of the URISA 2nd Caribbean GIS conference, Barbados, Caribbean, 209-219

Coe, M. T., Costa, M. H., & Howard, E. A. (2008). Simulating the surface waters of the Amazon River basin: Impacts of new river geomorphic and flow parameterizations. *Hydrological Processes*, *22*(14), 2542–2553. https://doi.org/10.1002/hyp.6850

Congalton, R. G. (1991). A review of assessing the accuracy of classifications of remotely sensed data. *Remote Sensing of Environment*, *37*(1), 35–46.

DLR (German Aerospace Center) (2018). Global 3D elevation model from the TanDEM-X mission now freely available, DLR. Retrieved from https://www.dlr.de/dlr/en/desktopdefault.aspx/tabid-10081/151_read-30139/#/gallery/32238 (accessed 18th October, 2018).

Eckstein, D., Kunzel, V., & Schafer, L. (2017). Global climate risk index, 2018: Who suffers most from extreme weather events? Weather-related loss events in 2016 and 1997 to 2016, Germanwatch, Bonn, Germany.

Farr, T. G., Caro, E., Crippen, R., Duren, R., Hensley, S., Kobrick, M., et al. (2007). The Shuttle Radar Topography mission. *Reviews of Geophysics*, *45*, RG2004. https://doi.org/10.1029/2005RG000183

Fiji Bureau of Statistics (2010). Fiji census of population and housing, Fiji Bureau of Statistics, Suva, Fiji.

Fiji Bureau of Statistics (2018). 2017 population and housing census release 1: Age, sex, geography and economic activity, Fiji Bureau of Statistics, Suva, Fiji.

Geiß, C., Wurm, M., Breunig, M., Felbier, A., & Taubenböck, H. (2015). Normalization of TanDEM-X DSM data in urban environments with morphological filters. *IEEE Transactions on Geoscience and Remote Sensing*, *53*(8), 4348–4362. https://doi.org/10.1109/TGRS.2015.2396195

Gesch, D. B. (2009). Analysis of Lidar elevation data for improved identification and delineation of lands vulnerable to sea-level rise. *Journal of Coastal Research Special Issue*, *53*, 49–58.

Government of Fiji (2016). Post-disaster needs assessment: Tropical cyclone Winston, Government of Fiji, Suva, Fiji.

Government of Fiji (2017). Climate vulnerability assessment: Making Fiji climate resilient, Government of Fiji, Suva, Fiji.

Hay, J. E., & Mimura, N. (2013). Vulnerability, risk and adaptation assessment methods in the Pacific Islands region: Past approaches and considerations for the future. *Sustainability Science*, *8*(3), 391–405. https://doi.org/10.1007/s11625-013-0211-y

Hirt, C. (2018). Artefact detection in global digital elevation models (DEMs): The maximum slope approach and its application for complete screening of the SRTM v4.1 and MERIT DEMs. *Remote Sensing of Environment*, *207*, 27–41. https://doi.org/10.1016/j.rse.2017.12.037

Hirt, C., Filmer, M. S., & Featherstone, W. E. (2010). Comparison and validation of the recent freely available ASTER-GDEM ver1, SRTM ver4.1 and GEODATA DEM-9S ver3 digital elevation models over Australia. *Australian Journal of Earth Sciences*, *57*(3), 337–347. https://doi.org/10.1080/08120091003677553

Holland, P. (2014). Economic dimensions of improved meteorological services in the Pacific, South Pacific community, Suva, Fiji.

Horritt, M. S., & Bates, P. D. (2001). Effects of spatial resolution on a raster-based model of flood flow. *Journal of Hydrology*, *253*(1–4), 239–249. https://doi.org/10.1016/S0022-1694(01)00490-5

Hunter, N. M. (2005). Development and assessment of dynamic storage cell codes for flood inundation modelling, (PhD thesis). Bristol University of Bristol.

Hunter, N. M., Bates, P. D., Horritt, M. S., & Wilson, M. D. (2007). Simple spatially-distributed models for predicting flood inundation: A review. *Geomorphology*, *90*(3-4), 208–225. https://doi.org/10.1016/j.geomorph.2006.10.021

Jarihani, A. A., Callow, J. N., McVicar, T. R., Van Niel, T. G., & Larsen, J. R. (2015). Satellite-derived Digital Elevation Model (DEM) selection, preparation and correction for hydrodynamic modelling in large, low-gradient and data-sparse catchments. *Journal of Hydrology*, *524*, 489–506. https://doi.org/10.1016/j.jhydrol.2015.02.049

Jarvis, A., Reuter, H. I., Nelson, E., & Guevara, E. (2008). Hole-filled SRTM for the globe. *Version 4*. CGIAR-CSI Database. Retrieved from http://srtm.csi.cgiar.org (Accessed 3rd October 2017).

Jing, C., Shortridge, A., Lin, S., & Wu, J. (2013). Comparison and validation of SRTM and ASTER GDEM for a subtropical landscape in Southeastern China. *International Journal of Digital Earth*, *7*, 969–992.

Krieger, G., Moreira, A., Fiedler, H., Hajnsek, I., Werner, M., Younis, M., et al. (2007). TanDEM-X: A satellite formation for high-resolution SAR interferometry. *IEEE Transactions on Geoscience and Remote Sensing*, *45*(11), 3317–3341. https://doi.org/10.1109/TGRS.2007.900693

Lehner, B., Verdin, K., & Jarvis, A. (2008). New global hydrography derived from spaceborne elevation data. *Eos, Transactions of the American Geophysical Union*, *89*(10), 93–94. https://doi.org/10.1029/2008EO100001

Marks, K., & Bates, P. D. (2000). Integration of high resolution topographic data with floodplain flow models. *Hydrological Processes*, *14*(11-12), 2109–2122. https://doi.org/10.1002/1099-1085(20000815/30)14:11/12<2109::AID-HYP58>3.0.CO;2-1

Martone, M., Bräutigam, B., Rizzoli, P., Gonzalez, C., Backmann, M., & Krieger, G. (2012). Coherence evaluation of TanDEM-X interferometric data. *ISPRS Journal of Photogrammetry and Remote Sensing*, *73*, 21–29. https://doi.org/10.1016/j.isprsjprs.2012.06.006

Martone, M., Rizzoli, P., Wecklich, C., Gonzalez, C., Bueso-Bello, J.-L., Valdo, P., et al. (2018). The global forest/non-forest map from TanDEM-X interferometric SAR data. *Remote Sensing of Environment*, *205*, 352–373. https://doi.org/10.1016/j.rse.2017.12.002

Mason, D. C., Schumann, G., & Bates, P. D. (2011). Data utilization in flood inundation modelling. In G. Pender & H. Faulkner (Eds.), *Flood risk science and management* (pp. 211–233). Hoboken, NJ: Wiley-Blackwell.

Mason, D. C., Trigg, M., Garcia-Pintado, J., Cloke, H. L., Neal, J. C., & Bates, P. D. (2016). Improving the TanDEM-X Digital Elevation Model for flood modelling using flood extents from Synthetic Aperture Radar images. *Remote Sensing of Environment*, *173*, 15–28. https://doi.org/10.1016/j.rse.2015.11.018

Mataki, M., Koshy, K. C., & Lal, M. (2006). Baseline climatology of Viti Levu (Fiji) and current climatic trends. *Pacific Science*, *60*(1), 49–68. https://doi.org/10.1353/psc.2005.0059

McAneney, J., van den Honert, R., & Yeo, S. (2017). Stationarity of major flood frequencies and heights on the Ba River, Fiji, over a 122-year record. *International Journal of Climatology*, *37*, 171–178. https://doi.org/10.1002/joc.4989

Merz, B., Hall, J., Disse, M., & Schumann, A. (2010). Fluvial flood risk management in a changing world. *Natural Hazards and Earth System Sciences*, *10*(3), 509–527. https://doi.org/10.5194/nhess-10-509-2010

Mitchell, A. L., Lucas, R. M., Donnelly, B. E., Pfitzner, K., Milne, A. K., & Finlayson, M. (2007). A new map of mangroves for Kakadu National Park, Northern Australia, based on stereo aerial photography. *Aquatic Conservation: Marine and Freshwater Ecosystems*, *17*(5), 446–467. https://doi.org/10.1002/aqc.818

Moreira, A. (2017). The Tan-DEM-X mission: A new measurement of the Earth's topography and much more, the 18th International Radar Symposium 2017, Prague.

National Aeronautics and Space Administration (2017). NASA damage map aids Puerto Rico Hurricane response, National Aeronautics and Space Administration. Retrieved from https://www.nasa.gov/feature/jpl/nasa-damage-map-aids-puerto-rico-hurricane-response (Accessed 1st June, 2018).

Neal, J., Schumann, G., & Bates, P. (2012). A subgrid channel model for simulating river hydraulics and floodplain inundation over large and data sparse areas. *Water Resources Research*, *48*, W11506. https://doi.org/10.1029/2012WR012514

Nurse, L. A., McLean, R. F., Agard, J., Briguglio, L. P., Duvat-Magnan, V., Pelesikoti, N., et al. (2014). 'Small islands', In: Intergovernmental Panel on Climate Change. In *Climate change 2014: Impacts, adaptation, and vulnerability. Part B: Regional aspects. Contribution of Working Group II to the Fifth Assessment Report of the Intergovernmental Panel on Climate Change* (pp. 1613–1654). Cambridge, UK: Cambridge University Press.

O'Loughlin, F. E., Paiva, R. C. D., Durand, M., Alsdorf, D. E., & Bates, P. D. (2016). A multi-sensor approach towards a global vegetation corrected SRTM DEM product. *Remote Sensing of Environment*, *182*, 49–59. https://doi.org/10.1016/j.rse.2016.04.018

Paiva, R. C. D., Collischonn, W., & Tucci, C. E. M. (2011). Large scale hydrologic and hydrodynamic modelling using limited data and a GIS based approach. *Journal of Hydrology*, *406*(3–4), 170–181. https://doi.org/10.1016/j.jhydrol.2011.06.007

Pappenberger, F., Frodsham, K., Beven, K., Romanowicz, R., & Matgen, P. (2007). Fuzzy set approach to calibrating distributed flood inundation models using remote sensing observations. *Hydrology and Earth System Sciences*, *11*(2), 739–752. https://doi.org/10.5194/hess-11-739-2007

Pelling, M., & Uitto, J. I. (2001). Small island developing states: Natural disaster vulnerability and global change. *Environmental Hazards*, *3*, 49–62.

Pickup, G., & Warner, R. (1976). Effects of hydrologic regime on magnitude and frequency of dominant discharge. *Journal of Hydrology*, *29*(1-2), 51–75. https://doi.org/10.1016/0022-1694(76)90005-6

R Core Team (2018). R: A language and environment for statistical computing version 3.5.1, R Core Team. Retrieved from https://www.r-project.org/ (accessed 16th September 2018).

Rabus, B., Eineder, M., Roth, A., & Bamler, R. (2003). The Shuttle Radar Topography mission—A new class of Digital Elevation Models acquired by spaceborne radar. *ISPRS Journal of Photogrammetry and Remote Sensing*, *57*(4), 241–262. https://doi.org/10.1016/S0924-2716(02)00124-7

Rexer, M., & Hirt, C. (2014). Comparison of free high resolution digital elevation data sets (ASTER GDEM2, SRTM v2.1/v4.1) and validation against accurate heights from the Australian National Gravity Database. *Australian Journal of Earth Sciences*, *61*(2), 213–226. https://doi.org/10.1080/08120099.2014.884983

Rexer, M., & Hirt, C. (2016). Evaluation of intermediate TanDEM-X digital elevation data products over Tasmania using other digital elevation models and accurate heights from the Australian National Gravity Database. *Australian Journal of Earth Sciences*, *62*(5), 599–609.

Richards, J. (1999). *Remote sensing digital image analysis* (pp. 1–240). Berlin, Germany: Springer-Verlag.

Rizzoli, P., Martone, M., Gonzalez, C., Wecklich, C., Borla Tridon, D., Bräutigam, B., et al. (2017). Generation and performance Assessment of the global TanDEM-X Digital Elevation Model. ISPRS. *Journal of Photogrammetry and Remote Sensing*, *132*, 119–139.

Rodriguez, E., Morris, C. S., & Belz, J. E. (2006). A global assessment of the SRTM performance. *Photogrammetric Engineering and Remote Sensing*, *72*(3), 249–260. https://doi.org/10.14358/PERS.72.3.249

Sampson, C. C., Smith, A. M., Bates, P. D., Neal, J. C., & Trigg, M. A. (2016). Perspectives on open access high resolution Digital Elevation Models to produce global flood hazard layers. *Frontiers in Earth Science*, *3*(85). https://doi.org/10.3389/feart.2015.00085

Sanders, B. F. (2007). Evaluation of on-line DEMs for flood inundation modeling. *Advances in Water Resources*, *30*(8), 1831–1843. https://doi.org/10.1016/j.advwatres.2007.02.005

Savage, J. T. S., Bates, P., Freer, J., Neal, J., & Aronica, G. (2015). When does spatial resolution become spurious in probabilistic flood inundation predictions. *Hydrological Processes*, *30*(13), 2014–2032.

Schreyer, J., Geiß, C., & Lakes, T. (2016). TanDEM-X for large-area modeling of urban vegetation height: Evidence from Berlin, Germany. *IEEE Journal of Selected Topics in Applied Earth Observations and Remote Sensing*, *9*(5), 1876–1887. https://doi.org/10.1109/JSTARS.2015.2508660

Schumann, G., Bates, P. D., Horritt, M. S., Matgen, P., & Pappenberger, F. (2009). Progress in integration of remote sensing-derived flood extent and stage data and hydraulic models. *Reviews of Geophysics*, *47*, RG4001. https://doi.org/10.1029/2008RG000274

Schumann, G. J. P., Bates, P. D., Neal, J. C., & Andreadis, K. M. (2014). Technology: Fight floods on a global scale. *Nature*, *507*(7491), 169. https://doi.org/10.1038/507169e

Simard, M., Pinto, N., Fisher, J. B., & Baccini, A. (2011). Mapping forest canopy height globally with spaceborne lidar. *Journal of Geophysical Research*, *116*, G04021. https://doi.org/10.1029/2011JG001708

Smith, A., Sampson, C., & Bates, P. (2015). Regional flood frequency analysis at the global scale. *Water Resources Research*, *51*, 539–553. https://doi.org/10.1002/2014WR015814

Stephens, E., Schumann, G., & Bates, P. D. (2014). Problems with binary pattern measures for flood model evaluation. *Hydrological Processes*, *28*(18), 4928–4937. https://doi.org/10.1002/hyp.9979

Thomas, B. (2012). Nadi LiDAR survey report for the Secretariat of the South Pacific Community Applied Geoscience and Technology Division (SOPAC), Network mapping aerial laser survey, Suva, Fiji.

United Nations (2015). Small island developing states in numbers: Climate change edition 2015, UN Office of the High Representative of the Least Developed Countries and Small Island Developing States, Geneva, Switzerland.

United Nations International Strategy for Disaster Reduction (2015). Global assessment report on disaster risk reduction 2015, United Nations International Strategy for Disaster Reduction, Geneva, Switzerland.

Wessel, B. (2016). TanDEM-X ground segment DEM products specification document, Earth observation center, DLR, Oberpfaffenhofen, Germany.

Wessel, B., Huber, M., Wohlfart, C., Marschalk, U., Kosmann, D., & Roth, A. (2018). Accuracy assessment of the global TanDEM-X Digital Elevation Model with GPS data. *ISPRS Journal of Photogrammetry and Remote Sensing*, *129*, 171–182.

Wilson, M. C., Bates, P. D., Alsdorf, D., Forsberg, B., Horritt, M. S., Melack, J., Frappart, F., et al. (2007). Modelling large-scale inundation of Amazonian seasonally flooded wetlands. *Geophysical Research Letters*, *34*, L15404. https://doi.org/10.1029/2007GL030156

Woodward, D. E., Hoeft, C. C., Humpal, A., Cerrelli, G. (2010). Chapter 15: Time of concentration, In: United States Department of Agriculture, 2010, *Part 630 – Hydrology: National Engineering Handbook*. Washington, DC.

Yamazaki, D., Baugh, C. A., Bates, P. D., Kanae, S., Alsdorf, D. E., & Oki, T. (2012). Adjustment of a spaceborne DEM for use in floodplain hydrodynamic modeling. *Journal of Hydrology*, *436-437*, 81–91. https://doi.org/10.1016/j.jhydrol.2012.02.045

Yamazaki, D., Ikeshima, D., Tawatari, R., Yamaguchi, T., O'Loughlin, F., Neal, J. C., et al. (2017). A high-accuracy map of global terrain elevations. *Geophysical Research Letters*, *44*, 5844–5853. https://doi.org/10.1002/2017GL072874

Yeo, S. (2015). Refining the historical flood series for Ba, Fiji, Risk Frontiers Technical Report, Macquarie University, Australia.

Yeo, S. W., Blong, R. J., & McAneney, J. (2007). Flooding in Fiji: Findings from a 100-year historical series. *Hydrological Sciences*, *52*(5), 1004–1015. https://doi.org/10.1623/hysj.52.5.1004

Zhang, J., Chen, S. H., Whitmann, D., Shyu, M.-L., & Zhang, C. (2003). A progressive morphological filter for removing non-ground measurements from airborne LIDAR data. *IEEE Transactions on Geoscience and Remote Sensing*, *41*(4), 872–882. https://doi.org/10.1109/TGRS.2003.810682